Ab Initio Multiple Spawning Dynamics Using Multi-State Second-Order Perturbation Theory

Hongli Tao,[†] Benjamin G. Levine,[‡] and Todd J. Martínez*,[†]

Department of Chemistry, Stanford University, Stanford, California, 94305, and Department of Chemistry, University of Pennsylvania, Philadelphia, Pennsylvania 19104

Received: July 6, 2009; Revised Manuscript Received: October 7, 2009

We have implemented multi-state second-order perturbation theory (MS-CASPT2) in the ab initio multiple spawning (AIMS) method for first-principles molecular dynamics including nonadiabatic effects. The nonadiabatic couplings between states are calculated numerically using an efficient method which requires only two extra energy calculations per time step. As a representative example, we carry out AIMS-MSPT2 calculations of the excited state dynamics of ethylene. Two distinct types of conical intersections, previously denoted as the twisted-pyramidalized and ethylidene intersections, are responsible for ultrafast population transfer from the excited state to the ground state. Although these two pathways have been observed in prior dynamics simulations, we show here that the branching ratio is affected by dynamic correlation with the twisted-pyramidalized intersection overweighting the ethylidene-like intersection during the decay process at the AIMS-MSPT2 level of description.

1. Introduction

Ab initio molecular dynamics (AIMD) is a powerful way to study molecular systems,[1,2] especially for nonadiabatic events or bond rearrangements that are difficult to describe with empirical potentials. The ab initio multiple spawning (AIMS) method[3] has been developed as a means of including quantum mechanical effects of the nuclei, especially those associated with nonadiabatic transitions or "surface crossing," in AIMD. The AIMS method solves for the electronic and nuclear wave functions simultaneously, as dictated by the molecular dynamics. In principle, AIMS can be applied to any multiple electronic state problem, as long as the underlying electronic structure method can provide an accurate description of the rapid changes in the electronic wave function during nonadiabatic events. In practice, it is highly advantageous that analytic energy gradients and nonadiabatic couplings are available to decrease the computational effort. We have previously shown that AIMS can be used with equation of motion coupled-cluster (EOM-CCSD) and multireference configuration interaction (MR-CI) methods.[1,4,5] Although these methods are expected to provide an accurate description of the electronic structure, the lack of implemented analytic expressions for the nonadiabatic coupling matrix elements (since remedied[6,7] in the case of MRCI) made extensive applications with this level of electronic structure theory difficult. Thus, we have often used state-averaged complete active space self-consistent field[8] (CASSCF) as the electronic structure method paired with the dynamics in AIMS.[9−11] Because CASSCF does not describe dynamic electron correlation efficiently, CASSCF-AIMS requires careful calibration and validation of the active space and the number of electronic states included in the state averaging.[12,13] An alternative method that is now recognized as one of the most accurate and efficient wave function-based techniques for excited electronic states is multistate second-order multireference perturbation theory (MSPT2).[14] The multistate variant allows the electronic states to mix after dynamic correlation effects have been incorporated through perturbation theory. This eliminates the "double-crossing' problems[14] that plague single-state second-order perturbation theory[15,16] (SS-CASPT2).

Until recently, the lack of implemented analytic expressions for the energy gradient and nonadiabatic coupling made it difficult to apply MSPT2 within the AIMS context (although it has been used for optimizations,[17−19] which typically require far fewer energy and gradient evaluations than dynamics). The introduction of analytic gradients for MSPT2 wave functions[20] has made it possible to consider MSPT2-AIMS simulations, and we have reported excited state dynamics calculations.[21] However, a remaining problem has been the lack of analytic expressions for the nonadiabatic coupling vector. In this paper, we show that only two projections of the nonadiabatic coupling vector are actually necessary for AIMS and how these can be efficiently determined using numerical finite difference techniques. We exploit this to carry out MSPT2-AIMS simulations of excited state dynamics for the ethylene molecule.

2. Theory

The AIMS method solves the electronic and nuclear Schrödinger equations simultaneously using a time-dependent adaptive nuclear basis set. The total wave function in AIMS is written as a sum of products of electronic and nuclear wave functions

$$\psi(r, R, t) = \sum_I \chi_I(R, t)\phi_I(r;R) \tag{1}$$

where the index I denotes the electronic state, $\phi_I(r;R)$ is the electronic wave function of state I, $\chi_I(R,t)$ is the time-dependent nuclear wave function associated with the Ith electronic state, and the electronic and nuclear coordinates are respectively referred to as r and R. The nuclear wave functions $\chi_I(R,t)$ are each given as superpositions of frozen Gaussian basis functions[22]

* To whom correspondence should be addressed. E-mail: Todd.Martinez@stanford.edu.
[†] Stanford University.
[‡] University of Pennsylvania.

10.1021/jp9063565 CCC: $40.75
Published on Web 11/04/2009

centered on classical trajectories, i.e., "trajectory basis functions" or TBFs

$$\chi_I(R,t) = \sum_i^{N_I(t)} c_I^i(t)\chi_I^i\left(R;\bar{R}_I^i(t),\bar{P}_I^i(t),\gamma_I^i(t)\right) \tag{2}$$

where N_I(t) is the number of basis functions associated with the Ith electronic state, $c_I^i(t)$ is the complex amplitude for the ith TBF on the Ith electronic state, and $\bar{R}_I^i(t)$, $\bar{P}_I^i(t)$, and $\gamma_I^i(t)$ are the position, momentum, and phase that parametrize the frozen Gaussian basis function. The position and momentum parameters of each of the TBFs are chosen to evolve according to Hamilton's equations for the associated electronic state, while the phase evolves according to the semiclassical prescription. Inserting the ansatz of eqs 1 and 2 into the time-dependent Schrödinger equation yields the equations of motion for the complex amplitudes that govern population transfer (both interelectronic state and intraelectronic state)

$$\sum_{Jj} S_{IJ}^{ij}\dot{c}_J^j + \dot{\bar{S}}_{IJ}^{ij}c_J^j = -i\sum_{Jj} H_{IJ}^{ij}c_J^j \tag{3}$$

where we have introduced the overlap, right-acting time derivative, and Hamiltonian matrix elements given in an orthonormal electronic basis as

$$\begin{aligned} S_{IJ}^{ij} &= \langle\chi_I^i|\chi_J^j\rangle_R\delta_{IJ} \\ \dot{\bar{S}}_{IJ}^{ij} &= \langle\chi_I^i|\frac{\partial}{\partial t}\chi_J^j\rangle_R\delta_{IJ} \\ H_{IJ}^{ij} &= \langle\chi_I^i\phi_I|\hat{H}|\chi_J^j\phi_J\rangle_{R,r} \\ &= \langle\chi_I^i|\hat{T}_{\text{nuc}}|\chi_J^j\rangle_R\delta_{IJ} + \langle\chi_I^i\langle\phi_I|\hat{H}_{el}|\phi_J\rangle_r\chi_J^j\rangle_R + 2D_{IJ}^{ij} + G_{IJ}^{ij} \end{aligned} \tag{4}$$

The Hamiltonian operator in eq 4 includes both nuclear and electronic terms and the nuclear kinetic energy and electronic Hamiltonian operators have been denoted as $\hat{T}_{\text{nuc}}$ and $\hat{H}_{\text{el}}$, respectively. The last two terms in the Hamiltonian matrix element promote nonadiabatic transitions due to the breakdown of the Born−Oppenheimer approximation

$$\begin{aligned} (\vec{d}_{IJ})_\rho &= \left\langle\phi_I\left|\frac{\partial}{\partial\boldsymbol{R}_\rho}\right|\phi_J\right\rangle_r \\ D_{IJ}^{ij} &= \sum_{\rho=1}^{3N}\left\langle\chi_I^i\left|d_{IJ,\rho}\frac{1}{2m_\rho}\frac{\partial}{\partial\boldsymbol{R}_\rho}\right|\chi_J^j\right\rangle_{r,R} \\ G_{IJ}^{ij} &= \sum_{\rho=1}^{3N}\frac{1}{2m_\rho}\left\langle\chi_I^i\left|\left\langle\phi_I\left|\frac{\partial^2}{\partial\boldsymbol{R}_\rho^2}\right|\phi_J\right\rangle_r\right|\chi_J^j\right\rangle_R \end{aligned} \tag{5}$$

where ρ indexes the Cartesian nuclear coordinates and we have defined the nonadiabatic coupling vector $\vec{d}_{IJ}$. The effect of the last term, G_{IJ}^{ij}, is typically quite minor, and thus it is usually neglected.

The kinetic energy, overlap, and right-acting time-derivative matrix elements required in AIMS can be (and are) evaluated analytically. However, analytic evaluation cannot be employed for the potential energy and nonadiabatic coupling matrix elements since there is no global analytic form for the potential energy surface and/or coupling terms in AIMS. Thus, we use a saddle-point approximation (SPA) to evaluate the potential energy matrix elements

$$\begin{aligned} V_{IJ}(R) &= \langle\phi_I(r;R)|\hat{H}_{el}|\phi_J(r;R)\rangle_r \\ \langle\chi_I^i\phi_I|\hat{H}_{el}|\chi_J^j\phi_J\rangle_{r,R} &= \langle\chi_I^i|V_{IJ}|\chi_J^j\rangle_R \approx \langle\chi_I^i|\chi_J^j\rangle_R V_{IJ}(\vec{R}_{\text{centroid}}) \\ (\vec{R}_{\text{centroid}})_\rho &= \frac{\alpha_I^\rho R_I^\rho + \alpha_J^\rho R_J^\rho}{\alpha_I^\rho + \alpha_J^\rho} \end{aligned} \tag{6}$$

This is the first term in a Taylor expansion about the center of the product TBF (R_{centroid}) and is motivated by the localized nature of the TBFs and TBF products. In principle, its accuracy can be improved by including more terms in the Taylor expansion. A similar saddle-point approximation is applied to the nonadiabatic coupling matrix elements that promote interelectronic state transitions

$$D_{IJ}^{ij} \approx \sum_{\rho=1}^{3N}(\vec{d}_{IJ}(\vec{R}_{\text{centroid}}))_\rho\langle\chi_I^i|\frac{1}{2m_\rho}\frac{\partial}{\partial R_\rho}\chi_J^j\rangle \equiv \vec{d}_{IJ,\text{centroid}}\vec{v}_{IiJj} \tag{7}$$

where we have introduced a generalized velocity matrix element $\vec{v}_{IiJj}$ and the nonadiabatic coupling matrix element is evaluated at the centroid geometry.

From the above, it is clear that AIMS requires as input the potential energy surface, gradients, and nonadiabatic coupling matrix elements at up to N_{TBF}^2 arbitrary nuclear positions (coordinate centers of all TBFs and TBF pairs) for each time step. The values of the potential energy surfaces and their analytical gradients can be obtained with the MSPT2 method as implemented, for example, in MolPro.[23] Analytic expressions for the nonadiabatic coupling vectors have not yet been implemented, so we now consider how these can be evaluated efficiently by finite difference. A key point is that, within the saddle point approximation embodied by eq 7, we only require a specific projection of the nonadiabatic coupling vector for any given pair of TBFs. This projection is a dot product of the real-valued nonadiabatic coupling vector with a complex-valued "velocity" vector and thus two independent projections of the nonadiabatic coupling vector are required to obtain the real and imaginary parts. With this observation, it is clear that finite difference is required along only two of the $3N$ possible directions for each of the D_{IJ}^{ij} matrix elements. Furthermore, the localized nature of the TBFs ensures all of the off-diagonal matrix elements, not only D_{IJ}^{ij} but also the off-diagonal kinetic and potential energy matrix elements, become negligible when the two TBFs involved are distant in phase space. The absolute value of the overlap matrix element between two TBFs, $|\langle\chi_I^i|\chi_J^j\rangle_R|$, is easily computed and can be monitored to avoid calculating potential energies when the final matrix element will be negligible. If the absolute value of the overlap matrix element for a given pair of TBFs falls below a numerical threshold, all off-diagonal matrix elements between this pair of TBFs are neglected. The energy gap between electronic states is also monitored and nonadiabatic coupling vectors are only computed if this gap falls below 0.6 eV (otherwise they are assumed to be negligibly small). These thresholding procedures significantly reduce the computational effort for the calculations.

The MS-CASPT2 wave function can be written as

$$|\phi_I^{\mathrm{MS-CASPT2}}\rangle = \sum_{p=1}^{M} C_{Ip}|\phi_p^{\mathrm{SS-CASPT2}}\rangle \tag{8}$$

where $\phi_p^{\mathrm{SS\text{-}CASPT2}}$ are single-state CASPT2 wave functions that will be recombined to form the MS-CASPT2 wave function, C_{Ip} are the mixing coefficients, and M is the total number of states which will be mixed. An effective Hamiltonian matrix and the corresponding overlap matrix ($\mathbf{H}^{\mathrm{MSPT2}}$ and $\mathbf{S}^{\mathrm{MSPT2}}$) in the space of SS-CASPT2 wave functions are constructed and the resulting generalized eigenvalue problem is solved to determine the mixing coefficients, as has been discussed previously.[14,24] The nonadiabatic coupling vector for the MSPT2 wave function is defined as

$$\begin{aligned}\vec{d}_{IJ} &= \left\langle \phi_I^{\mathrm{MS-CASPT2}}\left|\frac{\partial}{\partial \vec{R}}\right|\phi_J^{\mathrm{MS-CASPT2}}\right\rangle = \\ &\sum_{p,q}^{M}\frac{\partial C_{Jq}}{\partial \vec{R}}C_{Ip}\langle\phi_p^{\mathrm{SS-CASPT2}}|\phi_q^{\mathrm{SS-CASPT2}}\rangle + \\ &C_{Ip}C_{Jp}\left\langle\phi_p^{\mathrm{SS-CASPT2}}\left|\frac{\partial}{\partial \vec{R}}\right|\phi_q^{\mathrm{SS-CASPT2}}\right\rangle\end{aligned} \tag{9}$$

The integral in the second term in eq 9 can be further written as

$$\begin{aligned}&\left\langle\phi_p^{\mathrm{SS-CASPT2}}\left|\frac{\partial}{\partial \vec{R}}\right|\phi_q^{\mathrm{SS-CASPT2}}\right\rangle = \\ &\left\langle\phi_p^{\mathrm{CASSCF}} + \delta\phi_p^{\mathrm{PT2}}\left|\frac{\partial}{\partial \vec{R}}\right|\phi_q^{\mathrm{CASSCF}} + \delta\phi_q^{\mathrm{PT2}}\right\rangle = \\ &\left\langle\phi_p^{\mathrm{CASSCF}}\left|\frac{\partial}{\partial \vec{R}}\right|\phi_q^{\mathrm{CASSCF}}\right\rangle + \left\langle\delta\phi_p^{\mathrm{PT2}}\left|\frac{\partial}{\partial \vec{R}}\right|\phi_q^{\mathrm{CASSCF}}\right\rangle + \\ &\left\langle\phi_p^{\mathrm{CASSCF}}\left|\frac{\partial}{\partial \vec{R}}\right|\delta\phi_q^{\mathrm{PT2}}\right\rangle + \left\langle\delta\phi_p^{\mathrm{PT2}}\left|\frac{\partial}{\partial \vec{R}}\right|\delta\phi_q^{\mathrm{PT2}}\right\rangle\end{aligned} \tag{10}$$

Straightforward numerical implementation of eq 10 can be problematic because of the singular behavior of the CASSCF nonadiabatic coupling (first term on the third line), which needs to be canceled when CASSCF and MS-CASPT2 conical intersections are not located at the same geometries. A more stable approach is to work in the basis of diabatized CASSCF states. In this case, one must ensure that not only the CASSCF orbitals but also the CASSCF configuration interaction coefficients are chosen to change smoothly with molecular geometry.[25] If the CASSCF states (and therefore also the SS-CASPT2 states, provided the perturbation is small) are diabatized appropriately, all terms in eq 10 are effectively minimized and can be neglected. The diabatic coupling terms between SS-CASPT2 states are included in the off-diagonal elements of the MS-CASPT2 calculations. Therefore, the dominant nonadiabatic coupling contribution comes from the mixing coefficients at MS-CASPT2 level. In this case, the final form for the numerical nonadiabatic coupling between two adiabatic MS-CASPT2 states is

$$\begin{aligned}(\vec{d}_{IJ})_\rho &= \left\langle\phi_I^{\mathrm{MS-CASPT2}}\left|\frac{\partial}{\partial R_\rho}\right|\phi_q^{\mathrm{MS-CASPT2}}\right\rangle \\ &\approx \sum_{p,q}^{M}\frac{\Delta C_{Jq}}{\Delta R_\rho}C_{Ip}\langle\phi_p^{\mathrm{SS-CASPT2}}|\phi_q^{\mathrm{SS-CASPT2}}\rangle = \\ &\qquad \sum_{p,q}^{M}\frac{\Delta C_{Jq}}{\Delta R_\rho}C_{Ip}S_{pq}^{\mathrm{MS-CASPT2}}\end{aligned} \tag{11}$$

where we calculate the derivative of the mixing coefficient numerically

$$\begin{aligned}(\vec{d}_{IJ})_\rho &= \sum_{p,q}^{M}\frac{\Delta C_{Jq}}{\Delta R_\rho}C_{Ip}S_{pq} = \\ &\qquad \sum_{p,q}^{M}\frac{C_{Jq}(R_\rho + \Delta R_\rho) - C_{Jq}(R_\rho)}{\Delta R_\rho}C_{Ip}S_{pq}\end{aligned} \tag{12}$$

Since only the projection is required in eq 7, the final expression (shown for the real part only, the imaginary part is analogous)

$$\begin{aligned}\vec{e}_v^{\,\mathrm{Re}} &= \mathrm{Re}(\vec{v}_{IiJj}) \,/\, |\mathrm{Re}(\vec{v}_{IiJj})| \\ \mathrm{Re}(D_{IJ}^{ij}) &= |\mathrm{Re}(\vec{v}_{IiJj})| \times \\ &\sum_{p,q}^{M}\frac{C_{Jq}(\vec{R} + \varepsilon\vec{e}_v^{\,\mathrm{Re}}) - C_{Jq}(\vec{\mathrm{R}})}{\varepsilon}C_{Ip}(\vec{\mathrm{R}})S_{pq}(\vec{\mathrm{R}})\end{aligned} \tag{13}$$

where ε is a small finite step size. We choose ε such that the maximum atomic displacement is 0.01 bohr in this work.

The nonadiabatic coupling vector is used in three ways in AIMS. First, it is used to construct the Hamiltonian matrix elements as discussed above. Second, it is used to monitor impending nonadiabatic events. Specifically, when the magnitude of the nonadiabatic coupling at the center of a TBF exceeds a predefined threshold, the basis set is adaptively increased, i.e., spawning occurs. The lack of the complete nonadiabatic coupling vector causes no difficulties here, because one can instead monitor the magnitude of the nonadiabatic coupling vector projected along the TBF velocity. The third way in which the nonadiabatic coupling vector enters the AIMS formalism is in the selection of the parameters defining the child TBF which is spawned. We require that the classical energy of the parent and child TBFs be identical in order to ensure classical energy conservation in the long time limit when all TBFs have separated. Some adjustment of the momentum for the child TBF is typically needed to satisfy this constraint. There has been considerable discussion of such momentum adjustment procedures in related surface hopping methods,[26] and the usual procedure is to adjust the momentum along the nonadiabatic coupling vector. This procedure has been justified semiclassically by Herman.[27] The AIMS method is less sensitive to the details of this adjustment procedure since the basis functions have finite coordinate and momentum space width and population transfer proceeds through the solution of the time-dependent Schrödinger equation in this basis set. Furthermore, it is possible to allow both position and momentum adjustments in AIMS, and this freedom has been exploited recently to define an "optimal" spawning algorithm.[28] In the present work, we adjust the momentum along the direction defined by the energy difference gradient as a simple alternative to adjustment along the nonadiabatic coupling vector. Such an adjustment has been

used also in surface hopping methods previously[29] and in the present context avoids the need to compute all components of the nonadiabatic coupling vector.

3. Results and Discussion

As a test case for AIMS-MSPT2, we investigate the photodynamics of ethylene after $\pi \rightarrow \pi^*$ excitation. Ethylene is a paradigmatic molecule for photoinduced cis−trans isomerization in unsaturated hydrocarbons, and it has been studied extensively both experimentally[30,31] and theoretically.[1,2,32] The absorption spectrum of ethylene in the vacuum ultraviolet region is well understood from both experimental[33−35] and theoretical[36−38] studies. A number of Rydberg states appear in the low energy region, including at least one which lies below the $\pi \rightarrow \pi^*$ excited state. It is commonly thought that the Rydberg states play a minor role in the photochemical dynamics, but this remains to be firmly established. The vertical excitation energy for the $\pi \rightarrow \pi^*$ excited state is experimentally determined[39] to be 7.66 eV.

In the AIMS simulations described here, we use the MS-CASPT2 method with two electrons in two orbitals and state-averaged over the lowest three singlet states with a 6-31G* basis set, i.e., SA-3-CAS(2/2)-MSPT2/6-31G*. The vertical excitation energy for the $\pi \rightarrow \pi^*$ state is 8.62 eV, a significant improvement over the value of 10.12 eV obtained with the underlying CASSCF wave function, i.e., SA-3-CAS(2/2)/6-31G*. The improvement comes from inclusion of dynamic correlation in MS-CASPT2. However, there is still some discrepancy between the theoretical and experimental values. Angeli has recently argued that this is due to contraction of the π orbitals after the inclusion of dynamic electron correlation between σ and π electrons.[40] The chosen MS-CASPT2 wave function ansatz is therefore limited to describing the valence states (N, V, and Z in Mulliken nonmenclature[41]), but this is expected to be sufficient for photochemical mechanisms.

The dynamics started from the bright $\pi\pi^*$ state (S_1 in the MSPT2 ansatz used) and were followed for 250 fs. The final results were obtained by averaging over 13 different initial conditions generated by random sampling from the $v = 0$ Wigner distribution in the harmonic approximation. After vertical photoexcitation, ethylene relaxes by stretching and twisting around the C═C bond. The molecule evolves further to reach a region of high nonadiabatic coupling between the excited and the ground states, where new nuclear basis functions are spawned. Overall, 155 nuclear basis functions were spawned during the simulation time, i.e., an average of 12 per initial condition. More than 97% of the population is transferred to the ground electronic state by the end of the simulations.

The electronic population as a function of time is shown in Figure 1. Fitting to an exponential shows that the excited state lifetime from MS-CASPT2 dynamics is 89 ± 3 fs. We have also carried out AIMS simulations using the SA-3-CAS(2/2)/6-31G* electronic structure method in order to assess the role of dynamic electron correlation. The S_1 lifetime from AIMS-MSPT2 is somewhat shorter than the AIMS-CASSCF lifetime of 110 ± 6 fs, also shown in Figure 1. In both AIMS-MSPT2 and AIMS-CASSCF, the ultrafast population transfer indicates internal conversion via conical intersections. In fact, this has been discussed extensively, and there are two classes of intersections that are known to be important in the photodynamics.[1,2,9,13,32,42−44] The first class are twisted-pyramidalized geometries where the molecule is twisted about the C═C bond and pyramidalized about one of the C atoms. The second class is comprised of ethylidene-like (CH_3−CH) geometries where a

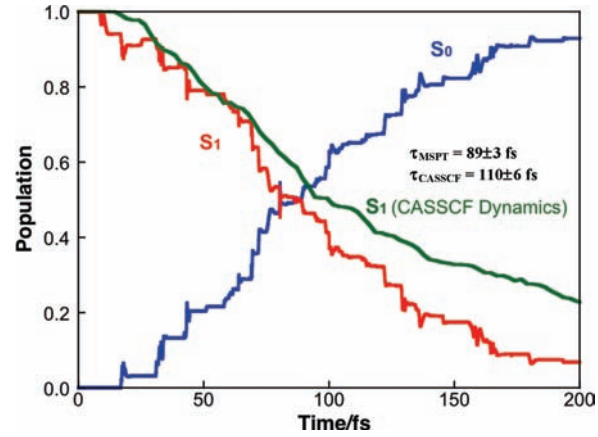

Figure 1. Population transfer from the excited state to the ground state, using SA3-MS-CAS(2/2)-PT2 (red and blue lines) and SA3-CAS(2/2) (green line).

H atom has migrated from one side of the molecule to the other. Minimal energy conical intersection (MECI) geometries for both classes have been obtained at the MS-CASPT2 level using our CIOpt penalty function based intersection optimization program.[19] The resulting MECI geometries for these two intersection classes are shown in Figure 2 along with superpositions of the spawning geometries that fall into each of these classes. The spawning geometries are defined as the centroid of the spawned Gaussian basis functions and provide a picture of the types of molecular geometries that dominate the nonadiabatic transitions.

In the AIMS-CASSCF dynamics, the twisted-pyramidalized and ethylidene-like conical intersections each account for about half of the population that is transferred to the ground electronic state. This result is in agreement with previous simulations of ethylene photodynamics that either neglected dynamic electron correlation[13] or modeled it implicitly with reparameterized semiempirical methods.[32] Although the same general types of intersections are involved in the AIMS-MSPT2 dynamics, the partitioning between these is different based on our dynamics data. Specifically, the twisted-pyramidalized intersection plays a bigger role in the decay mechanism. This is shown in Figure 3, where the pie chart in the inset shows the distribution of population transferred through the different intersections. As can be seen from the spawning geometries collected in Figure 2, there is rarely any ambiguity concerning which type of intersection is involved. However, for completeness, we note that this classification was done by computing a best alignment (by translation and rigid rotation) for each spawning geometry with each of the two MECIs (twisted-pyramidalized and ethylidene-like) and then assigning the type according to which comparison led to the lowest rms deviation.

The upper panel of Figure 3 is a histogram of the amount of population transferred as a function of the minimum energy gap between S_1 and S_0 during a nonadiabatic event. The histogram is separated out according to spawning events that proceed through twisted-pyramidalized or ethylidene-like conical intersections. In both cases, there is a propensity for increased population transfer when the energy gap is lower, as expected. However, dynamical effects are significant, and this is not a simple exponential decay with energy gap. This shows that both the energy gap and the manner in which the intersection seam is approached are important in determining the efficiency of population transfer. The lower panel of Figure 3 shows a similar histogram, but with the average percentage of the parent basis function population that is transferred instead of the absolute

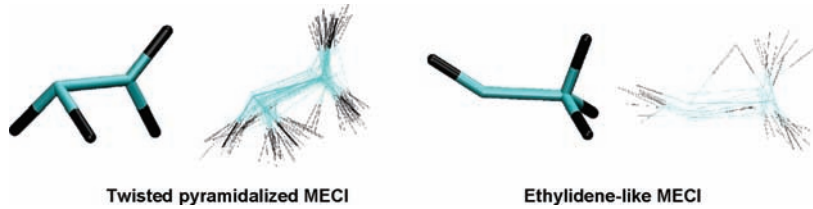

Figure 2. The two classes of S_1/S_0 intersections (twisted-pyramidalized and ethylidene-like), which are responsible for mediating electronic population transfer in ethylene. In each case, we show the MECI optimized with MS-CASPT2 (licorice-style structure) and a representative subset of the spawning geometries for the given intersection class (as a superposition of line structures).

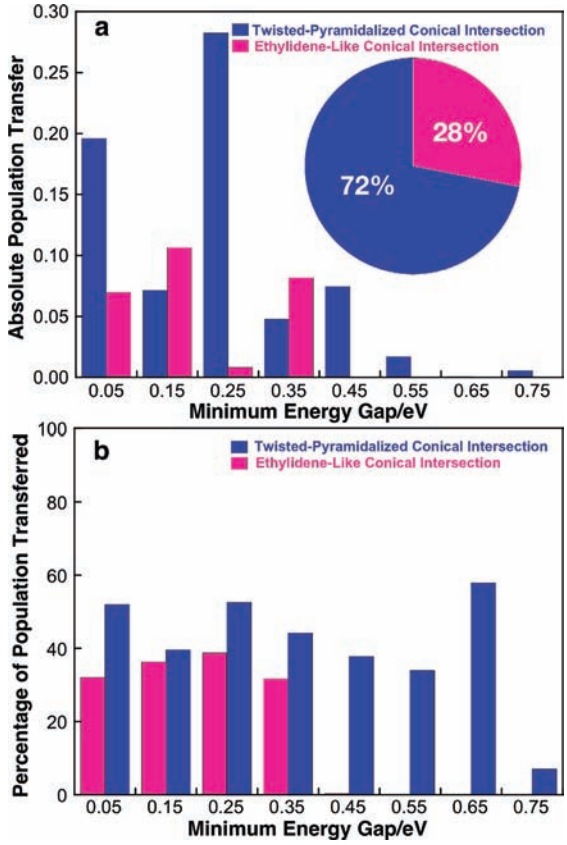

Figure 3. Population transfer as a function of the minimum S_1/S_0 energy gap during each spawning event. (a) Absolute amount of the population transferred via twisted-pyramidalized conical intersections (solid blue column) and ethylidene-like conical intersections (dotted blue column). The pie chart in the inset shows the fraction of population transferred to S_0 through the two different classes of intersections. (b) Average efficiency of population transfer as a function of the minimum S_1/S_0 energy gap during each spawning event for the two different classes of conical intersections. The efficiency is defined as the percentage of the parent TBF population which is transferred to its child TBF after the spawning event.

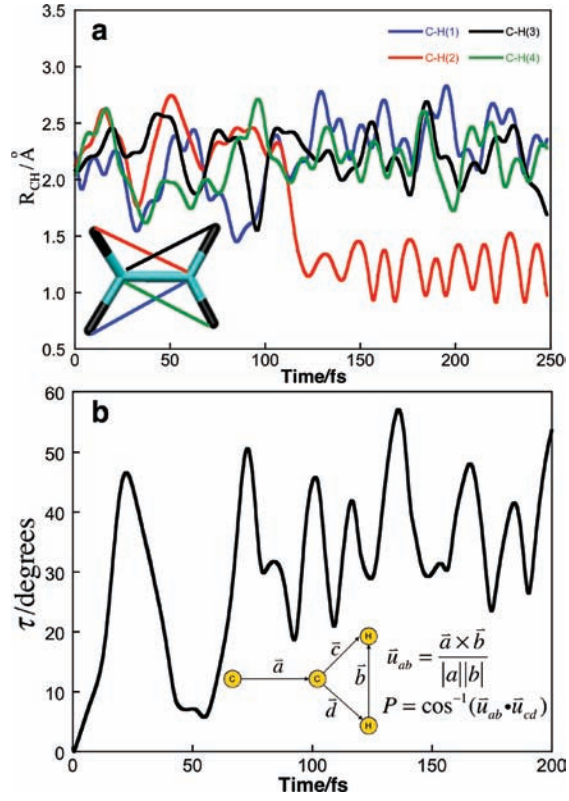

Figure 4. Dynamics of ethylene on S_1 for two representative trajectory basis functions (TBFs). (a) TBF which quenches through ethylidene-like conical intersections. The time evolution of the C—H bond distances are shown, emphasizing the migration of a H atom to form ethylidene. (b) TBF which quenches through twisted-pyramidalized conical intersections. The time evolution of the pyramidalization angle (defined in the inset) is shown.

population transfer. This might be expected to show a more pronounced peaked character around vanishing energy gap. However, it does not; if anything, the distribution is more nearly uniform (up to a cutoff energy gap). Again, this highlights the importance of dynamical effects in nonadiabatic phenomena. The apparent cutoff energy is much higher in the case of the twisted-pyramidalized intersection; there are nonadiabatic events that transfer a significant fraction of the parent basis function population even when the minimum energy gap accessed along the center of the TBF is as high as 0.65 eV. This is in contrast to the ethylidene-like intersection, where significant population transfer is not observed for minimal energy gaps exceeding 0.35 eV. This may be related to the fact that the twisted-pyramidalized intersection is strongly peaked, while the ethylidene-like intersection is sloped. This bears investigation in the future, but more initial conditions are needed for a detailed analysis. The role of intersection topography in population transfer has been previously discussed[45−49] but remains incompletely characterized.

In Figure 4, we show dynamical results for two representative TBFs that quench through the two different classes of intersections. The upper panel (Figure 4a) shows the time evolution of bond distances between carbon and hydrogen atoms that are not initially bonded. One of these distances suddenly drops from about 2 Å to about 1 Å, indicating the formation of an ethylidene-like structure and access to the ethylidene-like conical intersection. The lower panel (Figure 4b) shows the time evolution of the pyramidalization angle (defined in the inset) of the most pyramidalized carbon atom. This angle evolves from near zero to a large value, indicating pyramidalization of the carbon atom and access to the twisted-pyramidalized conical intersection.

After internal conversion to S_0 through either of the ethylidene-like or twisted-pyramidalized intersections, the ethylene

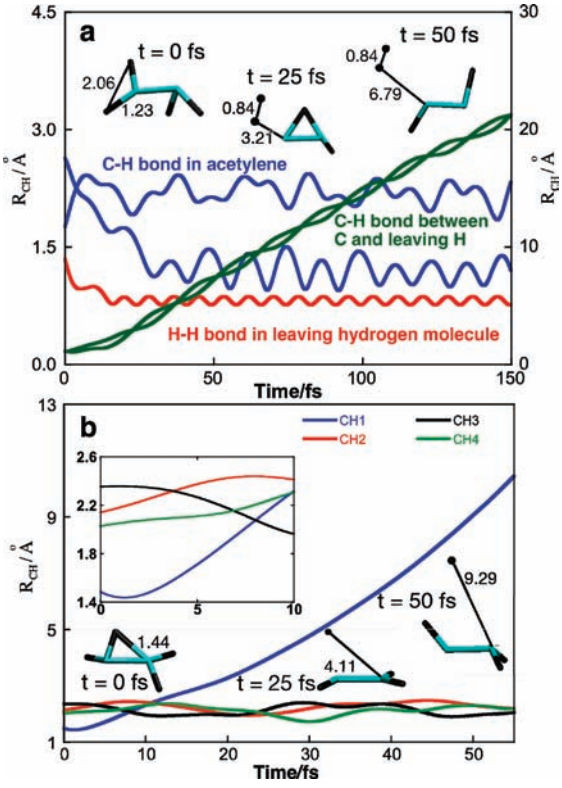

Figure 5. Dissociation reactions on S_0 after photoexcitation of ethylene. (a) Molecular elimination of H_2. The blue lines show the distances between carbon and hydrogen atoms that are not bonded initially. The red lines show the distance between the two departing hydrogen atoms, indicating the formation of hydrogen molecule (The bond length values are indicated by the left axis for blue and red lines). The dark green lines (values indicated by the right axis) show the bond distance between the departing hydrogen atoms and the carbon atom to which they were initially bonded (b) Atomic elimination of H atom. Distances between the carbon and hydrogen atoms which are not initially bonded are shown. The inset shows a blowup of the dynamics in the first 10 fs after the TBF was formed from quenching near a conical intersection. Snapshots of the molecular geometries with selected bond lengths are shown in both panels. The zero of time is the birth time of the spawned TBF in both panels.

molecule is highly vibrationally excited and multiple dissociation channels become energetically accessible. Previous experimental studies[50−52] pointed out four possible chemical dissociation channels.

$$C_2H_4 + h\nu \rightarrow HC{\equiv}CH + H_2 \quad (14\text{-a})$$

$$\rightarrow H_2C{\equiv}C: + H_2 \quad (14\text{-b})$$

$$\rightarrow H_2C{=}CH\cdot + H \quad (14\text{-c})$$

$$\rightarrow HC{\equiv}CH + 2H \quad (14\text{-d})$$

We observed both atomic and molecular elimination in the AIMS-MSPT2 dynamics simulations. Representative examples are shown in Figure 5. The upper panel (Figure 5a) shows molecular elimination of H_2 after quenching to S_0, leading directly to acetylene. The lower panel (Figure 5b) shows an example where an H atom dissociates to form vinylidene. As can be seen in the inset of Figure 5b, atomic elimination occurs after quenching through an ethylidene-like intersection in this

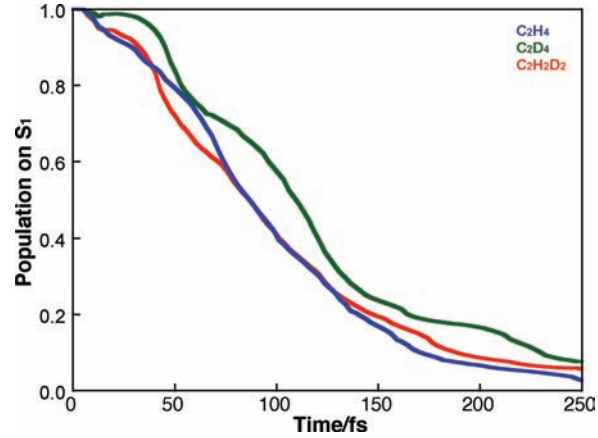

Figure 6. Excited-state population as a function of time for isotopomers of ethylene. Excited-state lifetimes obtained from a single exponential fit are denoted in the inset. Isotope substitution has little effect on the excited state lifetime in ethylene.

example. The occurrence of atomic and molecular elimination within our short simulation (200 fs) indicates that there may be nonstatistical character to the ground state dissociation reactions. This is supported by previous experiments,[53] which showed small angular anisotropy of the products of photodissociation of ethylene and its isotopic variants. Furthermore, an equilibrium Rice-Ramsperger-Kassel-Marcus calculation[54] yields significantly different results from experiments for the magnitude of the branching ratio and the wavelength-dependence of the molecular elimination channels.

We also investigated dynamics of deuterated isotopic variants of ethylene, $D_2C{=}CD_2$ and $D_2C{=}CH_2$. Simulation parameters are as described above for C_2H_4, with 15 initial conditions sampled for each isotopic variant. Experiments have reported[55,56] that the excited state lifetime is little affected by isotope substitution, which is somewhat surprising given the large role of hydrogen atom motion in the decay mechanism. As shown in Figure 6, our AIMS-MPST2 simulations predict negligible isotope effects (lifetimes vary between 89 and 110 fs for the three isotopic variants), in agreement with the experimental findings. Similar to ethylene, we observed H (D) and H_2 (HD/D_2) elimination on S_0 for both deuterated variants.

Conclusions

In summary, we have performed the first ab initio molecular dynamics using multistate second order perturbation theory (MS-CASPT2) with ethylene photodynamics as a test case. The results for ethylene are consistent with previous studies, but dynamic correlation effects lead to a shorter excited state lifetime and a higher preference for decay through twisted-pyramidalized conical intersections (as opposed to ethylidene-like conical intersections). Numerous fast fragmentation reactions (both atomic and molecular elimination) are observed on S_0 within 200 fs of excitation, suggesting that nonstatistical effects are important in determining the final branching ratios for the possible ground state products. The AIMS-MSPT2 simulations predict that isotope substitution has little effect on the excited state lifetime, in agreement with experiments but somewhat surprising given the intimate role of hydrogen atom motion in the decay mechanism. The excited state lifetime predicted by AIMS-MSPT2 (89 fs) is somewhat slower than the very fast (10−40 fs) lifetimes found in recent experiments.[31,55,56] It is possible that the Rydberg states play some role in accelerating the excited state decay, and this is a topic which bears further

investigation now that it is possible to carry out AIMS-MSPT2 simulations that include nonadiabatic and dynamic correlation effects.

The use of MS-CASPT2 in AIMS enables us to treat the electronic structure more accurately, especially when dynamic correlation is expected to be important in dynamics. We have outlined an approach which does not require evaluation of the full nonadiabatic coupling vectors, but instead uses finite differences along at most two directions for each trajectory basis function. This approach may be more effective than full evaluation of nonadiabatic coupling vectors even when these are available analytically since it avoids the necessity of solving the full coupled-perturbed CASPT2 equations.

Acknowledgment. This work was supported by the National Science Foundation (CHE-09-39169). A portion of the computational resources used was provided through DOE Contract DE-AC02-7600515.

References and Notes

(1) Ben-Nun, M.; Martinez, T. J. *Chem. Phys. Lett.* **1998**, *298*, 57.
(2) Ben-Nun, M.; Quenneville, J.; Martinez, T. J. *J. Phys. Chem. A* **2000**, *104*, 5161.
(3) Ben-Nun, M.; Martinez, T. J. *Adv. Chem. Phys.* **2002**, *121*, 439.
(4) Baeck, K. K.; Martinez, T. J. *Chem. Phys. Lett.* **2003**, *375*, 299.
(5) Choi, H.; Baeck, K. K.; Martinez, T. J. *Chem. Phys. Lett.* **2004**, *398*, 407.
(6) Lischka, H.; Dallos, M.; Szalay, P.; Yarkony, D. R.; Shepard, R. *J. Chem. Phys.* **2004**, *120*, 7322.
(7) Dallos, M.; Lischka, H.; Shepard, R.; Yarkony, D. R.; Szalay, P. G. *J. Chem. Phys.* **2004**, *120*, 7330.
(8) Roos, B. O. *Adv. Chem. Phys.* **1987**, *69*.
(9) Levine, B. G.; Martinez, T. J. *Annu. Rev. Phys. Chem.* **2007**, *58*, 613.
(10) Virshup, A. M.; Punwong, C.; Pogorelov, T. V.; Lindquist, B.; Ko, C.; Martinez, T. J. *J. Phys. Chem. B* **2009**, *113*, 3280.
(11) Martinez, T. J. *Acc. Chem. Res.* **2006**, *39*, 119.
(12) Coe, J. D.; Martinez, T. J. *J. Phys. Chem. A* **2006**, *110*, 618.
(13) Levine, B. G.; Coe, J. D.; Virshup, A. M.; Martinez, T. *J. Chem. Phys.* **2008**, *347*, 3.
(14) Finley, J.; Malmqvist, P. A.; Roos, B. O.; Serrano-Andres, L. *Chem. Phys. Lett.* **1998**, *288*, 299.
(15) Andersson, K.; Malmqvist, P.-A.; Roos, B. O. *J. Chem. Phys.* **1992**, *96*, 1218.
(16) Roos, B. O. *Acc. Chem. Res.* **1999**, *32*, 137.
(17) Hudock, H. R.; Levine, B. G.; Thompson, A. L.; Satzger, H.; Townsend, D.; Gador, N.; Ullrich, S.; Stolow, A.; Martinez, T. J. *J. Phys. Chem. A* **2007**, *111*, 8500.
(18) Hudock, H. R.; Martinez, T. J. *ChemPhysChem* **2008**, *9*, 2486.
(19) Levine, B. G.; Coe, J. D.; Martinez, T. J. *J. Phys. Chem. B* **2007**, *112*, 405.
(20) Celani, P.; Werner, H.-J. *J. Chem. Phys.* **2003**, *119*, 5044.
(21) Coe, J. D.; Levine, B. G.; Martinez, T. J. *J. Phys. Chem. A* **2007**, *111*, 11302.
(22) Heller, E. J. *J. Chem. Phys.* **1975**, *62*.
(23) Werner, H. J.; Lindh, P. J. K. R.; Manby, F. R.; Schütz, M. *MOLPRO, version 2006.1, a package of ab initio programs, see http://www.molpro.net.*
(24) Serrano-Andres, L.; Merchan, M.; Lindh, R. *J. Chem. Phys.* **2005**, *122*, 104107.
(25) In MolPro, this diabatization can be performed with the DIAB and DDR modules, for the orbitals and configuration interaction coefficients, respectively. Note that both of these procedures need to be performed in order to ensure fully diabatized CASSCF states.
(26) Preston, R. K.; Tully, J. C. *J. Chem. Phys.* **1971**, *54*.
(27) Herman, M. F.; Kluk, E. *Chem. Phys.* **1984**, *91*.
(28) Yang, S.; Coe, J. D.; Kaduk, B.; Martinez, T. J. *J. Chem. Phys.* **2009**, *130*, 134113.
(29) Blais, N. C.; Truhlar, D. G. *J. Chem. Phys.* **1983**, *79*, 1334.
(30) Collin, G. J. *Adv. Photochem.* **1987**, *14*, 135.
(31) Farmanara, P.; Stert, V.; Radloff, W. *Chem. Phys. Lett.* **1998**, *288*.
(32) Barbatti, M.; Ruckenbauer, M.; Lischka, H. *J. Chem. Phys.* **2005**, *122*, 174307.
(33) Wilkinson, P. G.; Mulliken, R. S. *J. Chem. Phys.* **1955**, *23*, 1895.
(34) Foo, P. D.; Innes, K. K. *J. Chem. Phys.* **1974**, *60*.
(35) Sension, R. J.; Hudson, B. S. *J. Chem. Phys.* **1989**, *90*.
(36) Rico, R. J.; Lee, T. J.; Head-Gordon, M. *Chem. Phys. Lett.* **1994**, *218*.
(37) Head-Gordon, M.; Rico, R. J.; Oumi, M. *Chem. Phys. Lett.* **1994**, *219*.
(38) Ryu, J.-S.; Hudson, B. S. *Chem. Phys. Lett.* **1995**, *245*.
(39) Johnson, K. E.; Johnson, D. B.; Lipsky, S. *J. Chem. Phys.* **1979**, *70*.
(40) Angeli, C. *J. Comput. Chem.* **2009**, *30*, 1319.
(41) Merer, A. J.; Mulliken, R. S. *Chem. Rev.* **1969**, *69*.
(42) Ohmine, I. *J. Chem. Phys.* **1985**, *83*, 2348.
(43) Freund, L.; Klessinger, M. *Int. J. Quantum Chem.* **1998**, *70*, 1023.
(44) Barbatti, M.; Granucci, G.; Persico, M.; Lischka, H. *Chem. Phys. Lett.* **2005**, *401*, 276.
(45) Ben-Nun, M.; Molnar, F.; Schulten, K.; Martinez, T. J. *Proc. Natl. Acad. Sci.* **2002**, *99*, 1769.
(46) Lee, A. M. D.; Coe, J. D.; Ullrich, S.; Ho, M.-L.; Lee, S.-J.; Cheng, B.-M.; Zgierski, M. Z.; Chen, I.-C.; Martinez, T. J.; Stolow, A. *J. Phys. Chem. A* **2007**, *111*, 11948.
(47) Yarkony, D. R. *J. Chem. Phys.* **2001**, *114*, 2601.
(48) Atchity, G. J.; Xantheas, S. S.; Ruedenberg, K. *J. Chem. Phys.* **1991**, *95*, 1862.
(49) Weingart, O.; Migani, A.; Olivucci, M.; Robb, M. A.; Buss, V.; Hunt, P. *J. Phys. Chem. A* **2004**, *108*, 4685.
(50) Sauer, M. J.; Dorfman, L. M. *J. Chem. Phys.* **1961**, *35*.
(51) Back, R. A.; Griffiths, W. L. *J. Chem. Phys.* **1967**, *46*.
(52) Okabe, H.; McNesby, J. R. *J. Chem. Phys.* **1962**, *36*.
(53) Lee, S. H.; Lee, Y. C.; Lee, Y. T. *J. Phys. Chem. A* **2006**, *110*.
(54) Chang, A. H. H.; Mebel, A. M.; Yang, X. M.; Lin, S. H.; Lee, Y. T. *J. Chem. Phys.* **1998**, *109*.
(55) Stert, V.; Lippert, H.; Ritze, H. H.; Radloff, W. *Chem. Phys. Lett.* **2004**, *388*, 144.
(56) Kosma, K.; Trushin, S. A.; Fuss, W.; Schmid, W. E. *J. Phys. Chem. A* **2008**, *112*, 7514.

JP9063565